Giant efficiency for charge-to-spin conversion via the electron gas at the $LaTiO_{3+\delta}/SrTiO_3$ interface

Jing Zhang,[1] Jine Zhang,[2] Xiang Chi,[1] Runrun Hao,[2] Weibin Chen,[2] Huaiwen Yang,[2] Dapeng Zhu,[2] Qinghua Zhang,[3] Weisheng Zhao,[2] Hui Zhang,[2,*] and Jirong Sun[1,3,4,5,*]

[1]*Songshan Lake Materials Laboratory, Dongguan, Guangdong 523808, People's Republic of China*
[2]*School of Integrated Circuit Science and Engineering, Beihang University, Beijing 100191, People's Republic of China*
[3]*Beijing National Laboratory for Condensed Matter Physics & Institute of Physics, Chinese Academy of Sciences, Beijing 100190, People's Republic of China*
[4]*School of Physical Sciences, University of Chinese Academy of Sciences, Beijing 100049, People's Republic of China*
[5]*Spintronics Institute, Jinan University, Jinan, Shandong 250022, People's Republic of China*

(Received 13 October 2021; revised 14 March 2022; accepted 21 April 2022; published 6 May 2022)

Spin-to-charge interconversion has been extensively investigated to improve its efficiency of charge-to-spin conversion, realizing magnetic switching by the technique of low-power spin-orbit torque (SOT). The quasi-two-dimensional electron gas (q2DEG) formed at the interface between insulating $SrTiO_3$ (STO) and $LaTiO_{3+\delta}$ (LTO) is supposed to possess strong Rashba spin-orbit coupling. Here, we show that a charge current flowing along the LTO/STO interface, which hosts a q2DEG, can efficiently generate a spin current, producing a strong SOT on adjacent NiFe layer as confirmed by spin-torque ferromagnetic resonance. The maximal charge-to-spin conversion efficiency is as large as ∼2.4 at room temperature, appearing in the NiFe/LTO/STO structure with a LTO thickness of 4 nm. This efficiency is much larger than that of heavy meals. With the decrease of temperature, the conversion efficiency only exhibits a slight decrease, remaining ∼1.5 at 20 K. The present work reveals the great potential of conducting oxide interface for oxide-based spintronics.

DOI: 10.1103/PhysRevB.105.195110

I. INTRODUCTION

Two-dimensional electron gases (2DEGs) at the interface of insulating oxides have attracted significant attention because of their unique physical properties that are potentially applicable, including ultrahigh mobility [1], interfacial magnetism [2] and superconductivity [3,4], gate tunable Rashba effect [5,6], and spin-to-charge interconversion [7–9]. Although the microscopic mechanism that leads to the 2DEGs is still under debate, there is no doubt that the 2DEGs will enable the innovation of spintronics. With the emergence of different 2DEGs, alternative approaches have been explored to get an effective tuning to carrier mobility and interfacial magnetism [10,11]. Based on the Edelstein effect and inverse Edelstein effect, recently spin-to-charge interconversion via the heterointerfaces has been reported [8,12–14], as an interesting topic for 2DEGs with strong spin-orbital coupling (SOC) [15–18]. Edelstein effect causes a transformation from charge current to spin current, while inverse Edelstein effect shows that a spin accumulation in 2DEGs will generate an in-plane electric field perpendicular to the direction of spin polarization. Inverse Edelstein effect has been observed by Song *et al.* [8] at room temperature and by Lesne *et al.* [14] at 7 K for the $LaAlO_3/SrTiO_3$ (LAO/STO) 2DEGs, with a high efficiency for spin-to-charge conversion. Recently, Wang *et al.* reported a giant charge-to-spin conversion for the STO/LAO system [7], an Edelstein effect. These works demonstrate the great potential of the oxide 2DEGs for the applications to spintronics.

In addition to LAO, $LaTiO_{3+\delta}$ (LTO) can also form a 2DEG at the LTO/STO interface. Compared with LAO, LTO shows several distinct features [19–22]. First, the unpaired Ti d^1 valence electron of Ti^{3+} forms an antiferromagnetic Mott-insulating state with a correlation gap of ∼0.2 eV [23,24]. The interfacial properties of LTO are thus expected to be influenced by electronic correlations that favor a magnetic ground state. Second, the Ti^{3+} states in LTO can readily accommodate additional holes so that a direct charge transferring from this state to the corresponding Ti^{4+} state of STO can occur at the LTO/STO interface. Third, LTO tends to extract oxygen from adjacent STO when it is deposited on STO at high temperatures [25], forming additional electron doping to STO. Therefore, even a single LTO/STO interface might be conductive [26,27].

Recently, strong Rashba SOC has been predicted for the d bands of the 2DEG at the LAO/STO interface [13–15]. These works show the possibility to electrically switch magnetization direction via the spin-orbit torque (SOT) of 2DEG. Although the effect of SOT has been reported for heavy metals such as Pt, Ta, and W [28–31], its efficiency is not high enough, and usually a very large current density is required, causing undesired side effects.

In this work, we present a systematic investigation on charge-to-spin conversion at different temperatures for the NiFe/LTO/STO devices with different LTO thicknesses. Based on the technique of spin torque ferromagnetic resonance (ST-FMR), the charge-to-spin conversion efficiency

*Corresponding authors: huizh@buaa.edu.cn; jrsun@iphy.ac.cn

was determined. For the NiFe/LTO (4 nm)/STO device, the SOT efficiency $|\theta_{CS}|$ is as large as 2.4 at room temperature, obtained with a frequency of 7 GHz. This efficiency is more than 1 order of magnitude higher than that of heavy metals (0.07 in Pt [28] and 0.3 in W [31]). It is also much larger than a previously reported value for a similar LTO/STO device [32]. With the decrease of temperature, the SOT efficiency exhibits a slow decrease. In addition to SOT efficiency, the Gilbert damping coefficient (α) and the effective magnetic field ($4\pi M_{\rm eff}$) were also determined. This work opens a promising window to manipulate magnetization using pure charge current, expanding the scope of SOT-based spintronic applications.

II. EXPERIMENTAL DETAILS

LTO layer was grown on a TiO_2-terminated STO (001) single crystalline substrate ($5\times5\times0.5\,\text{mm}^3$) by pulsed laser deposition (PLD). A KrF excimer laser ($\lambda = 248\,\text{nm}$) was employed. The repetition rate is 2 Hz and the fluence is $\sim2\,\text{J cm}^{-2}$. During the deposition process, the substrate temperature was set to 700 °C and the oxygen pressure was maintained at 1×10^{-5} mbar. After deposition, the temperature of the sample was furnace-cooled to room temperature. A total of four samples were fabricated, with LTO film thicknesses of 2, 4, 6, and 8 nm, respectively. The layer thickness was determined by deposition time which has been carefully calibrated. The resultant samples were taken out of the PLD chamber and then immediately transferred into a high vacuum chamber (base pressure lower than 2×10^{-8} mbar) to grow the NiFe layers with the thickness of 6 nm using magnetron sputtering at room temperature. From the PLD to the sputtering chambers, the sample was exposed to atmosphere for about 5 min. There is no special procedure for surface preparation. The sputtering pressure is 4×10^{-3} mbar. All samples were capped with a 3-nm SiO_2 layer to prevent samples from oxidation. In the transfer process, the LTO/STO was preserved in a vacuum tank and the transferring process was completed in a very short time. The lattice image of our sample was obtained by a scanning transmission electron microscope with double C_S correctors (STEM, JEOL-ARM200F). Using the technique of photolithography and dry etching, the multilayer films were patterned into standard Hall bars ($120\times10\,\mu\text{m}^2$) and rectangular-shaped strips ($20\times100\,\mu\text{m}^2$) for anisotropy magnetoresistance (AMR) and ST-FMR measurements, respectively. Au (100 nm)/Cr (10 nm) metal stacks were deposited as contacts for electrical measurements.

III. RESULTS AND DISCUSSION

A. Characterization of the LTO/STO heterostructures

We performed a STEM analysis of the typical sample. Figure 1(a) shows the high-angle annular dark-field (HAADF) lattice image of the cross section of NiFe (6 nm)/LTO (4 nm)/STO. Lattice sites can be clearly seen. The bright and faint dots in the LTO layer correspond to La and Ti, respectively. Moreover, the NiFe/LTO and LTO/STO interfaces are clear and sharp (marked by red lines), without obvious signatures of interlayer diffusion.

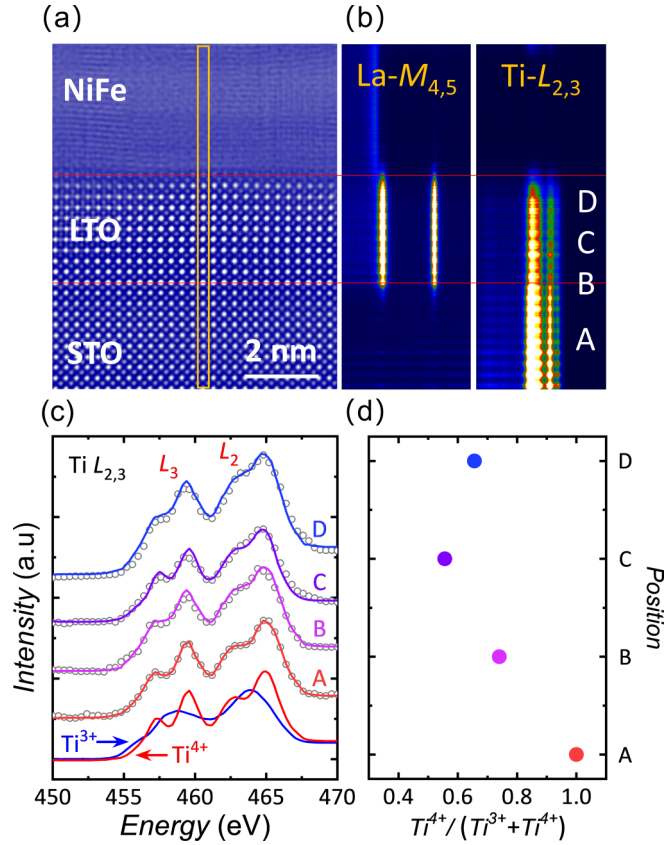

FIG. 1. (a) HAADF lattice image of the cross section of NiFe (6 nm)/LTO (4 nm)/STO, recorded along the [100] zone axis. Red lines mark interfaces. (b) Electron energy loss spectroscopy (EELS) spectrum image of the Ti-$L_{2,3}$ and La-$M_{4,5}$ edges, recorded along a vertical column marked in (a). (c) Line profiles of the Ti-$L_{2,3}$ EELS spectra obtained along different levels of the EELS spectrum image. For clarity, the EELS spectra have been differently upwards shifted. Symbols represent the experimental data, and the solid lines are results of curve fitting based on the two bottom curves that are standard reference spectra of Ti^{3+} and Ti^{4+}. (d) Ti^{4+} content versus vertical position.

To get the information about the valence state of the Ti ions in LTO, we also recorded the electron energy loss spectroscopy (EELS) spectrum. Figure 1(b) is the EELS spectrum images of the Ti-$L_{2,3}$ and La-$M_{4,5}$ edges. Line profile analysis along different levels of the EELS spectrum image yields a series the Ti-$L_{2,3}$ spectra [Fig. 1(c)]. The EELS spectra indicate that the valence state of the Ti ions in STO (position *A*) is +4. In contrast, the EELS spectra of the Ti ions in LTO exhibit the features of Ti^{3+} and Ti^{4+} ions, and can be fitted by combining the spectra of Ti^{3+} and Ti^{4+}. This result implies the coexistence Ti^{3+} and Ti^{4+} ions. A rough estimation based on curve fitting shows that the proportion of Ti^{4+} is about 56-74%, as shown in Fig. 1(d). This means a formula of $LaTiO_{3+\delta}$ for LTO with $\delta \approx 0.28$-0.37.

B. ST-FMR analysis of the LTO (4 nm)/STO device at different temperatures

ST-FMR measurement is an effective technique to evaluate the SOT efficiency. We show in Fig. 2(a) the schematic

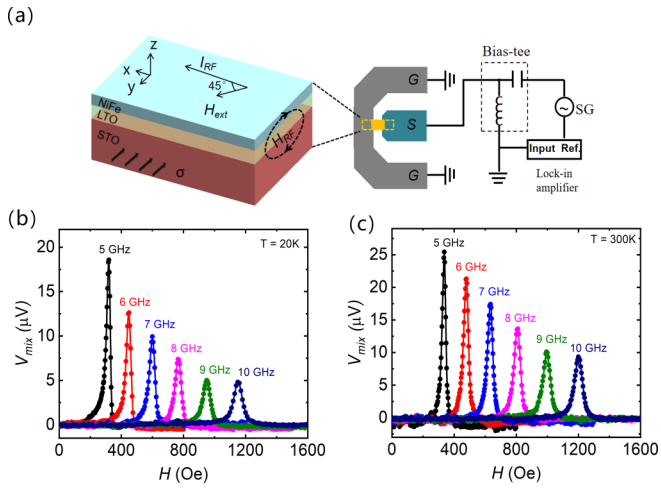

FIG. 2. (a) A schematic diagram for device details and the set up for ST-FMR measurements. (b),(c) ST-FMR spectra of the NiFe (6 nm)/LTO (4 nm)/STO device, collected at 20 and 300 K, respectively. Symbols are experimental data and solid lines are results of curve fitting.

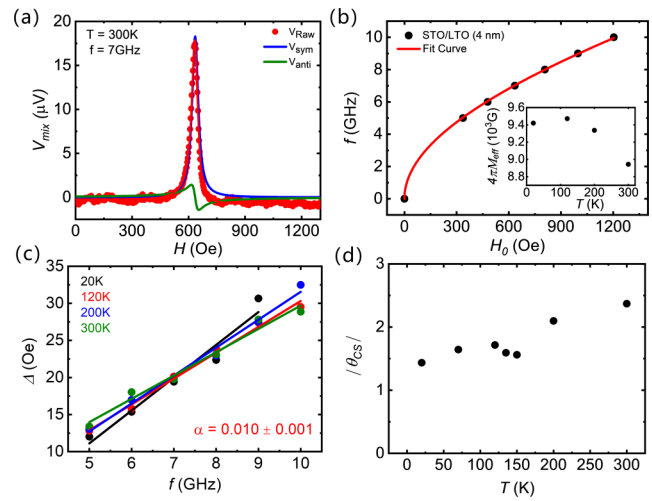

FIG. 3. (a) ST-FMR spectrum of the NiFe (6 nm)/LTO (4 nm)/STO device, obtained with 7 GHz at 300 K. (b) Resonant frequency f as a function of resonant field H_0. The solid curve represents the fitting results to Kittel formula. (c) Line width versus resonant frequency f, extracted from the curve fitting of the ST-FMR spectra obtained at different temperatures. Solid lines are results of linear fitting. The Δ-f slope defines the Gilbert damping coefficient. (d) Efficiency of charge-to-spin conversion (Js/Jc) at different temperatures.

diagram for the ST-FMR setup. In addition to the measuring circuit, the detailed structure of the NiFe/LTO/STO device can also be clearly seen. A microwave-frequency (GHz) charge current I_{RF} (15 dBm in power) from the signal generator was applied to the device, and the resulting DC voltage is simultaneously measured by a bias tee. An in-plane magnetic field with a fixed angle of $\theta_H = 45^\circ$ with respect to the current axis was applied and swept from 0 to 1600 Oe during the measurement. As shown by the left panel of Fig. 2(a), when an in-plane radio frequency current (I_{RF}) is applied to the LTO/STO 2DEG layer, nonequilibrium spins are generated by the Rashba-Edelstein effect [8,33]. These accumulated spins generate a spin current J_S in the out-of-plane direction, exerting a spin torque on the NiFe layer. The oscillating current-induced torque causes a precession of the magnetization of NiFe, yielding an oscillated resistance due to the AMR of the NiFe layer. The resonance line shape can be measured using a direct voltage V_{mix}. The ST-FMR spectra of the NiFe (6 nm)/LTO (4 nm)/STO device are shown in Figs. 2(b) and 2(c), recorded in the frequency range 5–10 GHz at a temperature between 20 and 300 K. The amplitude decreases as the frequency increases. Notably, the signals at 300 K are considerably larger than those at 20 K, which implies a higher SOT efficiency at 300 K. We also performed a control experiment for the bare NiFe layer (6 nm) and the effect is much weaker than that of the NiFe/LTO/STO sample (please see Fig. S1 in the Supplemental Material for the ST-FMR spectra of NiFe (6 nm)/STO [34]).

As an example, Fig. 3(a) presents the ST-FMR spectrum collected at 300 K at 7 GHz. Based on curve fitting, the symmetric (V_S) and antisymmetric (V_A) components of the spectrum can be determined. The measured curve can be well fitted by a Lorentzian function [35,36] consisting of a symmetric and an antisymmetric Lorentzian component as follows: $V_{\mathrm{mix}} = S\frac{\Delta^2}{\Delta^2+(H_{\mathrm{ext}}-H_0)^2} + A\frac{\Delta(H_{\mathrm{ext}}-H_0)}{\Delta^2+(H_{\mathrm{ext}}-H_0)^2}$, where Δ is the linewidth (full width at half maximum), H_0 is the resonant magnetic field, S and A are the symmetric and antisymmetric Lorentzian coefficients, respectively. By fitting the experiment results to this equation, the parameters Δ, S, A, and H_0 can be deduced. The amplitudes of symmetric (V_S) and antisymmetric (V_A) components are correlated with τ_{DL} and $(\tau_{FL} + \tau_{Oe})$, respectively. The resonance frequency f is shown in Fig. 3(b), as a function of resonance magnetic field H_0. f varies with H_0 following the Kittel relation: $f = (\gamma/2\pi)[H_0(H_0 + 4\pi M_{\mathrm{eff}})]^{1/2}$ [37], where γ is the gyromagnetic ratio. Based on the results of curve fitting, the effective magnetization ($4\pi M_{\mathrm{eff}}$) is determined to be ~9000 G for the NiFe layer. Please see Figs. S2 and S3 in the Supplemental Material for the analysis of the data collected below 300 K [34]. The inset plot in Fig. 3(b) presents the effective magnetization ($4\pi M_{\mathrm{eff}}$) as a function of temperature. $4\pi M_{\mathrm{eff}}$ decreases slightly with the increase of temperature. As the $4\pi M_{\mathrm{eff}}$ presents the contribution of interfacial anisotropy, these results indicate that with the increase of temperature the anisotropy decreases.

Information on magnetic damping can be identified from Fig. 3(c), where resonance peak width Δ is presented as a function of resonance frequency. Δ increases as the frequency increases for all temperatures. This parameter has intrinsic and extrinsic origins, and it is given by $\Delta = \Delta_0 + (2\pi\alpha/\gamma)f$, where Δ_0 is the extrinsic contribution (e.g., inhomogeneous broadening) to linewidth [37]. It is usually independent of frequency. The second term is the intrinsic contribution. It is linearly proportional to the frequency, with a slope proportional to Gilbert damping coefficient α. A direct calculation shows that the α is approximately 0.010 for the NiFe (6 nm)/LTO (4 nm)/STO device. This value matches well with the result of the NiFe film from spin valves [32]. As

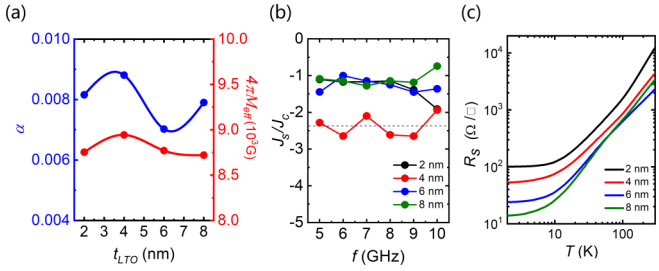

FIG. 4. (a) Gilbert damping coefficient and the effective magnetization values as functions of the thickness of LTO film. (b) Charge-to-spin conversion efficiency (J_S/J_C) at different frequencies. (c) Dependence of R_{sheet} on T of the samples with the LTO thicknesses of 2, 4, 6, and 8 nm, respectively.

temperature increases, the Gilbert damping coefficient decreases slightly (see Fig. S4 in the Supplemental Material for the fitting processes which leads to α at different temperatures). [34]

The SOT efficiency $|\theta_{CS}|$ in the NiFe/LTO/STO systems can be evaluated from the deduced S/A utilizing the following equation [37]:

$$|\theta_{CS}| = \left|\frac{J_S}{J_C}\right| = \left|\frac{S}{A}\right| \frac{e\mu_0 M_S t d}{\hbar}[1 + (4\pi M_{\text{eff}}/H_0)]^{1/2},$$

where J_S represents the spin current density injected into the NiFe layer, J_C (A/cm^2) is the uniform charge current density flowing through the LTO/STO 2DEG layer, M_S is the saturation magnetization of NiFe, t is the thickness of the NiFe layer, and d is the thickness of the 2DEG conducting layer. The SOT efficiency of NiFe (6 nm)/LTO (4 nm)/STO is presented in Fig. 3(d), as a function of temperature. $|\theta_{CS}|$ ranges ~1.5-2.4 as temperature varies, which is much larger than that reported by Yang *et al.* [32]. Notably, the SOT efficiency at 135 and 150 K is slightly smaller than that at other temperatures. The reason is unclear at present. It may be associated with the Jahn-Teller distortions of the LTO layer in this temperature range [38,39].

C. Efficiency of charge-to-spin conversion for devices with different LTO layers at room temperature

To clarify the evolution of the SOT efficiency with the thickness of LTO, we further measured the ST-FMR spectra for the devices with a LTO layer of 2, 6, and 8 nm, respectively. The Gilbert damping coefficient α and the effective magnetization ($4\pi M_{\text{eff}}$) are deduced (see Fig. S5 in the Supplemental Material for the detailed procedure of data analysis that leads to α and $4\pi M_{\text{eff}}$) [34]. As shown in Fig. 4(a), both α and $4\pi M_{\text{eff}}$ change slightly as the LTO thickness varies, forming a wave-shaped α-t_{LTO} ($4\pi M_{\text{eff}}$-t_{LTO}) curve . Notably, the maximal Gilbert damping coefficient and effective magnetization appear in the sample of NiFe (6 nm)/LTO (4 nm)/STO ($\alpha = 0.009$ and $4\pi M_{\text{eff}} = 8943$ G). For other samples, α and $4\pi M_{\text{eff}}$ fluctuate around 8720 and 8750 G, respectively. These results imply that the NiFe (6 nm)/LTO (4 nm)/STO sample has the highest charge-to-spin conversion efficiency. Figure 4(b) presents the deduced $|\theta_{CS}|$, as a function of frequencies. As expected, the 2, 6, and 8 nm LTO present a similar charge to spin efficiency with a value about 1.0, which is obviously smaller than that of a NiFe (6 nm)/LTO (4 nm)/STO device. Although the Js/Jc of different frequencies is oscillated, the NiFe (6 nm)/LTO (4 nm)/STO show apparently the highest charge-to-spin efficiency (~2.4). This efficiency is 1 or 2 orders of magnitude higher than that of heavy metals such as for Pt, Ta, and W, which have spin Hall angles between 0.06 and 0.30 [28–31].

Take the sample NiFe (6 nm)/LTO (6 nm)/STO as an example. We also tried to confirm the high SOT efficiency of the 2DEGs by using DC-biased ST-FMR technique [35] for which an additional DC was also applied along with I_{RF} to modulate the linewidth Δ. Unfortunately, we found that the ST-FMR spectrum of the 2DEG was strongly disturbed by applying an additional I_{DC} (± 1.0 mA) along with I_{RF} (see Fig. S6 in the Supplemental Material). Consequently, it is hard to obtain a linear fit between linewidth Δ and I_{DC} for 2DEG unlike for the Pt/Py system [35], i.e., we failed to confirm the charge-spin conversion efficiency using the current-induced enhanced damping method. A possible reason could be the large resistivity difference between 2DEG and Py (~3500 $\mu\Omega$ cm versus ~45 $\mu\Omega$ cm). In this case, the DC mainly flows through the Py layer, somehow disturbing the ST-FMR spectrum. It is different from the typical metal system Pt/Py, for which the resistivity difference between Pt and Py is much smaller (~20 $\mu\Omega$ cm versus ~45 $\mu\Omega$ cm) [35].

Notably, the performance of the best NiFe/LTO/STO device is similar to or even better than the emerging topological insulator Bi_2Se_3 which exhibits a SOT efficiency of ~0.43–3.5 [40,41]. Completely different from heavy metal materials, the charge-to-spin conversion of 2DEG at the LTO/STO interface is caused by spin-momentum locking. In this case, an electric current flowing along interface will generate a spin accumulation thus a perpendicular spin current, leading to charge-to-spin conversion. The spin-momentum locking is a consequence of the Rashba-typed spin splitting of the band structure of 2DEG. The larger the spin splitting is the stronger the spin-momentum locking thus the SOT efficiency will be. Usually, the spin splitting at the oxide interface can be very large. As reported, the Rashba spin splitting energy is about 10 meV for the LAO/STO interface [16] and as large as 30 meV for the LAO/KTO interface [17]. Therefore, the SOT efficiency of the conducting oxide interface could be unusually large.

Figure 4(c) demonstrates the temperature-dependent sheet resistance R_S of the LTO/STO heterostructures without a NiFe capping layer, recorded by van der Pauw geometry. The sheet resistance R_S decreases drastically as the temperature decreases and then almost saturates below 10 K. This temperature dependence implies a typical metallic behavior [1,10] of the 2DEG at the LTO/STO interface. Notably, the LTO (4 nm)/STO device demonstrates no difference with other samples. It means that the SOT efficiency is determined by the mechanism that is out of the capture of a simple electronic transport.

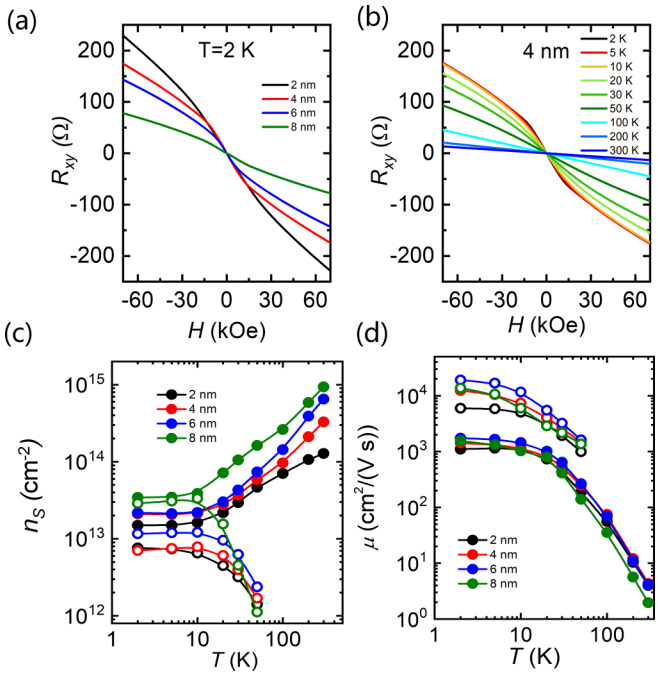

FIG. 5. (a) Dependence of R_{XY} on magnetic field H at 2 K with different LTO thickness. (b) Dependence of R_{XY} on magnetic field H at different temperatures with 4-nm LTO. Temperature dependence of the carrier density (c) and Hall mobility (d). The solid and hollow dots represent type one and type two charge carriers respectively.

D. Hall resistivity of the LTO/STO heterostructure without a NiFe capping layer

To get further information on 2DEGs with different LTO thickness, Hall resistivity is investigated. As shown in Fig. 5(a), all R_{xy}-H curves obtained at 2 K exhibit a deviation from linearity around 1.5 T. This feature enhances with the decrease of the LTO thickness. According to Fig. 5(b), the R_{xy}-H curves of LTO (4 nm)/STO behave differently and the deviation from linearity appears at about 50 K when cooled down from 300 K, which signifies the appearance of the second species of charge carriers. Meanwhile, the R_{xy}-H slope declines considerably with the increase of LTO thickness and temperature, implying a concomitant increase in carrier density. The complex R_{xy}-H relation is an indication of either the occurrence of nonlinear Hall effect or the appearance of more than one species of charge carriers.

We tried to fit the R_{xy}-H relation to the two-band model [42]:

$$R_{XY}(H) = -\frac{1}{e}\frac{\left(\frac{n_1\mu_1^2}{1+\mu_1^2H^2}+\frac{n_2\mu_2^2}{1+\mu_2^2H^2}\right)H}{\left(\frac{n_1\mu_1}{1+\mu_1^2H^2}+\frac{n_2\mu_2}{1+\mu_2^2H^2}\right)^2+\left(\frac{n_1\mu_1^2}{1+\mu_1^2H^2}+\frac{n_2\mu_2^2}{1+\mu_2^2H^2}\right)^2H^2}$$

with the constraint of

$$R_S(0) = \frac{1}{e(n_1\mu_1 + n_2\mu_2)},$$

where n_1 and n_2 demote, respectively, type one and type two sheet carriers at the LTO/STO interface, μ_1 and μ_2 are the corresponding Hall mobility, and e is electron charge. Obviously, $n_S = n_1$ when there is only one species of sheet carriers and $n_S = n_1 + n_2$ when two species of charge carriers coexist. The two band-model presents a good description of the Hall effect, allowing the determination of carrier density and corresponding Hall mobility. As shown in Figs. 5(c) and 5(d), when cooling down from 300 K, the density of the first species of charge carriers decreases rapidly. When temperature is below 50 K, the second species of charge carriers appears and its density increases with the further decrease of temperature from 50 K down to 10 K. Below 10 K, the carrier density saturates at a constant value that depends on the thickness of LTO.

For example, the charge carriers of LTO (4 nm)/STO decrease from 3.38×10^{14} to 1.98×10^{13} cm^{-2} when cooled from 300 to 2 K while the second charge carriers increase from 2.02×10^{12} to 6.98×10^{12} cm^{-2}. In contrast, the mobility grows rapidly upon cooling. Corresponding to temperature variation from 300 to 2 K, the mobility grows rapidly from ∼4.0 to ∼1400 cm^2/(V s) for the first species of charge carriers. The second species of charge carriers appears at 50 K, where they show the Hall mobility of ∼1400 cm^2/(V s). At 2 K, the highest mobility of ∼12 000 cm^2/(V s) is obtained for the second species of charge carriers. According to Wang *et al.* [7], the SOC strength in 2DEG is maximal when Fermi energy is around the Lifshitz point. In this case, the spin current can be effectively generated with a higher $|\theta_{CS}|$ in the 2DEG layer at low temperatures. Our ST-FMR measurements show that $|\theta_{CS}|$ becomes smaller at low temperatures [Fig. 3(d)]. This can be ascribed to the difficulty for the spin transmission through the LTO layer at low temperatures.

Notably, the carrier density of the 2DEG at the LTO/STO interface is generally one order of magnitude higher than that of the 2DEG at the LAO/STO interface. This could be a consequence of outward oxygen diffusion from STO to LTO. The high carrier density also implies a thick thickness of the conduction layer at the LTO/STO interface, i.e., the electron gas at the LTO/STO interface is actually quasi-two-dimensional.

IV. CONCLUSIONS

In summary, a giant charge-to-spin efficiency has been demonstrated for the NiFe/LTO/STO heterostructures in a wide temperature range from 20 to 300 K. The calculated charge-to-spin conversion efficiency $|\theta_{CS}|$ has values up to 2.4 for the sample of NiFe (6 nm)/LTO (4 nm)/STO, which verifies the strong SOC at the LTO/STO interface, suggesting that the LTO/STO can be a promising spin generator for practical applications. This value is much larger than that of Pt (0.07). Our results may greatly invigorate the field of room-temperature SOT-driven magnetization switching in ferromagnet/LTO/STO or ferrimagnet structures/LTO/STO, promoting the development of full oxide insulator-based spintronic devices.

ACKNOWLEDGMENTS

This work has been supported by the Science Center of the National Science Foundation of China (Grant No. 52088101), the National Key R&D Program of China (Grants No. 2018YFB0407602, No. 2017YFA0303601, No. 2017YFA0206300, No. 2018YFA0305704, No.

2019YFA0308401, and No. 2019YFA0704904), the National Natural Science Foundation of China (Grants No. 11934016, No. 12004022, No. 51972335, No. 12104027, and No. 12104029), the Key Program of the Chinese Academy of Sciences, the Beijing Municipal Science and Technology Project (Grant No. Z201100004220002), and the China Postdoctoral Science Foundation (Grant No. 2020M670085). J.R.S. is thankful for the support of the Project for Innovative Research Team of National Natural Science Foundation of China (Grant No. 11921004).

[1] G. Herranz, M. Basletic, M. Bibes, C. Carretero, E. Tafra, E. Jacquet, C. Deranlot K.Bouzehouane, A. Hamzic, J. M. Broto, A. Barthelemy, and A. Fert, Phys. Rev. Lett. **98**, 216803 (2007).

[2] A. Brinkman, M. Huijben, M. van Zalk, J. Huijben, U. Zeitler, J. C. Maan, G. Rijnders, W. G. van der Wiel, D. H. A. Blank, and H. Hilgenkamp, Nat. Mater. **6**, 493 (2007).

[3] L. Li, C. Richter, J. Mannhart, and R. C. Ashoori, Nat. Phys. **7**, 762 (2011).

[4] N. Reyren, S. Thiel, A. D. Caviglia, L. Fitting Kourkoutis, G. Hammerl, C. Richter, C. W. Schneider, T. Kopp, A.-S. Rüetschi, D. Jaccard, M. Gabay, D. A. Muller, J.-M. Triscone, and J. Mannhart, Science **317**, 1196 (2007).

[5] G. Singh, A. Jouan, S. Hurand, C. Feuillet-Palma, P. Kumar, A. Dogra, R. Budhani, J. Lesueur, and N. Bergeal, Phys. Rev. B **96**, 024509 (2017).

[6] M. Ben Shalom, M. Sachs, D. Rakhmilevitch, A. Palevski, and Y. Dagan, Phys. Rev. Lett. **104**, 126802 (2010).

[7] Y. Wang, R. Ramaswamy, M. Motapothula, K. Narayanapillai, D. P. Zhu, J. W. Yu, T. Venkatesan, and H. Yang, Nano Lett. **17**, 7659 (2017).

[8] Q. Song, H. R. Zhang, T. Su, W. Yuan, Y. Chen, W. Xing, J. Shi, J. R. Sun, and W. Han, Sci. Adv. **3**, e1602312 (2017).

[9] F. Trier, D. C. Vaz, P. Bruneel, P. Noël, A. Fert, L. Vila, J.-P. Attané, A. Barthélémy, M. Gabay, H. Jaffrès, and M. Bibes, Nano Lett. **20**, 395 (2020).

[10] A. F. Santander-Syro, O. Copie, T. Kondo, F. Fortuna, S. Pailhès, R. Weht, X. G. Qiu, F. Bertran, A. Nicolaou, A. Taleb-Ibrahimi, P. Le Fèvre, G. Herranz, M. Bibes, N. Reyren, Y. Apertet, P. Lecoeur, A. Barthélémy, and M. J. Rozenberg, Nature (London) **469**, 189 (2011).

[11] P. D. C. King, R. H. He, T. Eknapakul, P. Buaphet, S.-K. Mo, Y. Kaneko, S. Harashima, Y. Hikita, M. S. Bahramy, C. Bell, Z. Hussain, Y. Tokura, Z. X. Shen, H. Y. Hwang, F. Baumberger, and W. Meevasana, Phys. Rev. Lett. **108**, 117602 (2012).

[12] J. Y. Chauleau, M. Boselli, S. Gariglio, R. Weil, G. de Loubens, J.-M Triscone, and M. Viret, Europhys. Lett. **116**, 17006 (2016).

[13] D. C. Vaz, P. Noël, A. Johansson, B. Göbel, F. Y. Bruno, G. Singh, S. McKeown-Walker, F. Trier, L. M. V. Arche, A. Sander, S. Valencia, P. Bruneel, M. Vivek, M. Gabay, N. Bergeal, F. Baumberger, H. Okuno, A. Barthélémy, A. Fert, L. Vila *et al.*, Nat. Mater. **18**, 1187 (2019).

[14] E. Lesne, Y. Fu, S. Oyarzun, J. C. Rojas-Sánchez, D. C. Vaz, H. Naganuma, G. Sicoli, J.-P. Attané, M. Jamet, E. Jacquet, J.-M. George, A. Barthélémy, H. Jaffffrès, A. Fert, M. Bibes, and L. Vila, Nat. Mater. **15**, 1261 (2016).

[15] H. R. Zhang, Y. Yun, X. J. Zhang, H. Zhang, Y. Ma, X. Yan, F. Wang, G. Li, R. Li, T. Khan, Y. S. Chen, W. Liu, F. X. Hu, B. G. Liu, B. G. Shen, W. Han, and J. R. Sun, Phys. Rev. Lett. **121**, 116803 (2018).

[16] A. D. Caviglia, M. Gabay, S. Gariglio, N. Reyren, C. Cancellieri, and J. M. Triscone, Phys. Rev. Lett. **104**, 126803 (2010).

[17] H. Zhang, X. Yan, X. J. Zhang, S. Wang, C. M. Xiong, H. R. Zhang, S. J. Qi, J. E. Zhang, F. R. Han, N. Wu, B. G. Liu, Y. S. Chen, B. G. Shen, and J. R. Sun, ACS Nano **13**, 609 (2019).

[18] Z. Zhong, A. Toth, and K. Held, Phys. Rev. B **87**, 161102(R) (2013).

[19] F. D. Wen, Y. W. Cao, X. R. Liu, B. Pal, S. Middey, M. Kareev, and J. Chakhalian, Appl. Phys. Lett. **112**, 122405 (2018).

[20] I. Altfeder, H. Lee, J. J. Hu, R. D. Naguy, A. Sehirlioglu, A. N. Reed, A. A. Voevodin, and C. B. Eom, Phys. Rev. B **93**, 115437 (2016).

[21] J. S. Kim, S. S. A. Seo, M. F. Chisholm, R. K. Kremer, H.-U. Habermeier, B. Keimer, and H. N. Lee, Phys. Rev. B **82**, 201407(R) (2010).

[22] J. H. You and J. H. Lee, Phys. Rev. B **88**, 155111 (2013).

[23] H. Ishida and A. Liebsch, Phys. Rev. B **77**, 115350 (2008).

[24] V. R. Cooper, Phys. Rev. B **85**, 235109 (2012).

[25] P. Scheiderer, M. Schmitt, J. Gabel, M. Zapf, M. Stubinger, P. Schutz, L. Dudy, C. Schlueter, T. L. Lee, M. Sing, and R. Claessen, Adv. Mater. **30**, 1706708 (2018).

[26] J. Biscaras, N. Bergeal, S. Hurand, C. Grossetete, A. Rastogi, R. C. Budhani, D. LeBoeuf, C. Proust, and J. Lesueur, Phys. Rev. Lett. **108**, 247004 (2012).

[27] W. S. Choi, S. Lee, V. R. Cooper, and H. N. Lee, Nano Lett. **12**, 4590 (2012).

[28] I. M. Miron, K. Garello, G. Gaudin, P.-J. Zermatten, M. V. Costache, S. Auffret, S. Bandiera, B. Rodmacq, A. Schuhl, and P. Gambardella, Nature (London) **476**, 189 (2011).

[29] L. Liu,C. F. Pai, Y. Li, H. W. Tseng, D. C. Ralph, and R. A. Buhrman, Science **336**, 555 (2012).

[30] C. F. Pai, L. Liu, Y. Li, H. Tseng, D. Ralph, and R. Buhrman, Appl. Phys. Lett. **101**, 122404 (2012).

[31] X. Qiu, K. Narayanapillai, Y. Wu, P. Deorani, D. H. Yang, W. S. Noh, J. H. Park, K. J. Lee, H. Y. Lee, and H. Yang, Nat. Nanotechnol. **10**, 333 (2015).

[32] H. W. Yang, B. Y. Zhang, X. Y. Zhang, X. Yan, W. L. Cai, Y. L. Zhao, J. R. Sun, K. L. Wang, D. P. Zhu, and W. S. Zhao, Phys. Rev. Appl. **12**, 034004 (2019).

[33] V. M. Edelstein, Solid State Commun. **73**, 233 (1990).

[34] See Supplemental Material at http://link.aps.org/supplemental/10.1103/PhysRevB.105.195110 for additional ST-FMR signal of the NiFe (6 nm)/STO and NiFe (6 nm)/LTO (4 nm)/STO at different temperatures, and additional fitting processes to get the Gilbert damping coefficient and the effective magnetization of the samples under different temperatures or different LTO layer thickness.

[35] L. Q. Liu, T. Moriyama, D. C. Ralph, and R. A. Buhrman, Phys. Rev. Lett. **106**, 036601 (2011).

[36] A. R. Mellnik, J. S. Lee, A. Richardella, J. L. Grab, P. J. Mintun, M. H. Fischer, A. Vaezi, A. Manchon, E.-A. Kim, N. Samarth, and D. C. Ralph, Nature (London) **511**, 449 (2014).

[37] T. X. Nan, S. Emori, C. T. Boone, X. J. Wang, T. M. Oxholm, J. G. Jones, B. M. Howe, G. J. Brown, and N. X. Sun, Phys. Rev. B **91**, 214416 (2015).

[38] J. Hemberger, H. A. Krug von Nidda, V. Fritsch, J. Deisenhofer, S. Lobina, T. Rudolf, P. Lunkenheimer, F. Lichtenberg, A. Loidl, D. Bruns, and B. Büchner, Phys. Rev. Lett. **91**, 066403 (2003).

[39] L. Chen, C. Xu, H. Tian, H. J. Xiang, J. Íñiguez, Y. R. Yang, and L. Bellaiche, Phys. Rev. Lett. **122**, 247701 (2019).

[40] Y. Wang, P. Deorani, K. Banerjee, N. Koirala, M. Brahlek, S. Oh, and H. Yang, Phys. Rev. Lett. **114**, 257202 (2015).

[41] M. Jamali, J. S. Lee, J. S. Jeong, F. Mahfouzi, Y. Lv, Z. Zhao, B. K. Nikolic, K. A. Mkhoyan, N. Samarth, and J. P. Wang, Nano Lett. **15**, 7126 (2015).

[42] F. Gunkel, C. Bell, H. Inoue, B. Kim,A. G. Swartz, T. A. Merz, Y. Hikita, S. Harashima, H. K. Sato, M. Minohara, S. Hoffmann-Eifert, R. Dittmann, and H. Y. Hwang, Phys. Rev. X **6**, 031035 (2016).